BESTDR Enables Bayesian Quantification of Mechanism-Specific Drug Responses

Thomas O. McDonald[1,2,3,4], Simone Bruno[1,2,3], James P. Roney[5], Ioannis K. Zervantonakis[6], and Franziska Michor[1,2,3,4,7,8]

ABSTRACT

Understanding drug responses at the cellular level is essential for elucidating mechanisms of action and advancing preclinical drug development. Traditional dose–response models rely on simplified metrics, limiting their ability to quantify parameters like cell division, death, and transition rates between cell states. To address these limitations, we developed Bayesian Estimation of STochastic processes for Dose-Response (BESTDR), a framework modeling cell growth and treatment response dynamics to estimate concentration–response relationships using longitudinal cell count data. BESTDR enables quantification of rates in multistate systems across multiple cell lines using hierarchical modeling to support high-throughput screening. Validation of BESTDR with synthetic and experimental datasets demonstrates its accuracy and robustness in estimating drug response. By integrating mechanistic modeling of cytotoxic, cytostatic, and other drug effects, BESTDR enhances dose–response studies, facilitating robust drug comparisons and mechanism-specific analyses. BESTDR offers a versatile tool for early-stage preclinical research, paving the way for drug discovery and informed experimental design.

Significance: BESTDR leverages time-course cell count data to provide mechanistic insights into drug actions, distinguishing cytostatic, cytotoxic, and state transitions, thus advancing dose-response modeling crucial for preclinical research and development of targeted therapies.

This article is part of a special series: Driving Cancer Discoveries with Computational Research, Data Science, and Machine Learning/AI.

Introduction

In vitro cell culture experiments and dose–response modeling are fundamental tools in pharmacology and early drug development (1). These studies aim to quantify how drug concentration affects cell growth, guiding the identification of efficacious compounds and, when paired with molecular profiling, enabling discovery of biomarkers for drug response (2–5).

High-throughput drug screens test a range of compounds across panels of cell lines to prioritize candidates for further study (6–9). Increasingly, these experiments use real-time imaging to track live cell counts longitudinally (10, 11). These technologies support labeling of distinct phenotypes, such as apoptotic cell states (12), mutation status, epigenetic states (13, 14), and cell cycle phases (15). These multidimensional data provide an opportunity to better understand drug responses and cell kinetics, given appropriate statistical methods to incorporate multiple states and time points.

In traditional viability assays, drug response is modeled using relative cell count fold change as a function of drug concentration and summarized using statistics for efficacy (e.g., E_{max}) or potency (e.g., IC_{50}; refs. 16, 17). Recent modeling advances addressed changes in the concentration–response (CR) functional relationship. For example, DrFIT accounts for nonmonophasic concentration responses that deviate from the standard Hill function, leading to increased flexibility via a mixture of Hill functions accounting for multiple pathways (18). Gaussian processes can model the relationship between concentration and viability and account for experimental noise (19). Other studies employ Gaussian processes (20), neural networks, and machine learning methods (21) to better account for prediction variability. These methods still use cell counts as the response variable, which are sensitive to assay conditions and may not reflect the mechanisms of drug action such as cytostatic (i.e., inhibition) and cytotoxic (i.e., killing) effects (22, 23). For example, viability based on normalized cell counts cannot capture variability introduced by factors like stochasticity in cell cycle timing. To address these challenges, time-invariant metrics were developed that are robust to assay duration (22, 24); however, these metrics do not differentiate between drug mechanisms of action. Another approach estimates the cytotoxic and cytostatic responses with a Gaussian process for each drug response mechanism (25) but is restricted to single-cell states, limiting its use for complex response mechanisms. Although cell cycle models can reveal mechanism-specific effects (26), they are typically bespoke and lack a general framework linking drug concentration to dynamic rate changes.

Here, we present a novel framework, Bayesian Estimation of STochastic processes for Dose-Response (BESTDR), for quantifying drug effects on cell-kinetic mechanisms in culture. Using

---

[1]Department of Data Science, Dana-Farber Cancer Institute, Boston, Massachusetts. [2]Department of Biostatistics, Harvard T.H. Chan School of Public Health, Boston, Massachusetts. [3]Department of Stem Cell and Regenerative Biology, Harvard University, Cambridge, Massachusetts. [4]Center for Cancer Evolution, Dana-Farber Cancer Institute, Boston, Massachusetts. [5]Program in Computational and Systems Biology, Massachusetts Institute of Technology, Cambridge, Massachusetts. [6]Department of Bioengineering, UPMC Hillman Cancer Center, Swanson School of Engineering, University of Pittsburgh, Pittsburgh, Pennsylvania. [7]The Eli and Edythe L. Broad Institute, Cambridge, Massachusetts. [8]Ludwig Center at Harvard, Harvard Medical School, Boston, Massachusetts.

Corresponding Authors: Thomas O. McDonald, Dana-Farber Cancer Institute, 450 Brookline Avenue, Mailstop CLS-11007, Boston, MA 0221. E-mail: mcdonald@jimmy.harvard.edu; and Franziska Michor, michor@jimmy.harvard.edu

Cancer Res 2026;XX:XX–XX

doi: 10.1158/0008-5472.CAN-25-1181

longitudinal cell count data across concentrations (**Fig. 1A**), BESTDR models population growth as a branching process (27–29), in which individual cells stochastically divide, die, or switch states (**Fig. 1B**). Each fate occurs at a rate that can vary with drug concentration (**Fig. 1C**). From the data and model (**Fig. 1A** and **B**), BESTDR infers CR functions for each rate (**Fig. 1C**) by estimating their posterior distributions (**Fig. 1D**). These curves reveal mechanisms of action; for example, cytostatic and cytotoxic drugs may produce similar net growth yet differ in how they modulate division and death rates (**Fig. 1E**).

BESTDR also incorporates data from multiple cell states to model complex systems, such as cell cycle transitions or state switching (**Fig. 1F** and **G**), enabling drug-specific response estimation across growth, death, and transition mechanisms without added mathematical complexity (**Fig. 1H**). It supports high-throughput screens (HTS) via hierarchical modeling to account for variability across experiments or cell lines. By enabling flexible modeling of complex dynamics and handling of dataset heterogeneity, BESTDR is well suited for diverse applications. The R package is freely available on GitHub. In sum, BESTDR fills a gap in modeling drug effects on cell population dynamics by linking concentration to mechanism, an essential advance for early-phase drug development (15, 30).

Materials and Methods

Estimation of branching process parameters

The likelihood of a d-type continuous-time Markov Branching Process (CTMBP) at time t started by $\boldsymbol{N}$ individuals at time 0 is approximated by a d-dimensional multivariate normal distribution. This normal likelihood is justified because, in a CTMBP with a sufficiently large initial population, the distribution of cell counts at any given time approximates a normal distribution according to the Central Limit Theorem (28, 31). Given the starting individuals, time, and structure of the branching process, the mean and variance are numerically solved as a linear system of ordinary differential equations (see Supplementary Appendix for additional details). Because of the Markov property and time-homogeneity assumption, when multiple time points exist for the same trajectory, these are split up to act as individual samples, increasing the effective number of samples used to estimate the parameters.

The mean and variance at some time and a given concentration are both solved as functions of the starting number of individuals at the previous time, the estimates for all rates at that concentration, and the length of time between observations. As the variance is calculated from the stochastic process rather than representing a noise term, the variance in the data serves to help estimate additional parameters that would be unidentifiable using ordinary differential equation (ODE)–based methods that do not account for the variance. For example, populations with faster division and death rates exhibit higher variance in cell counts than those with the same net growth rate but slower rates; we leverage this variance to distinguish these rates.

When different drug concentrations are present in the data, a CR function $f_\theta(c)$ can be assumed for rate parameter θ with parameters $\theta_1, \theta_2, \ldots, \theta_k$. BESTDR estimates each of these parameters to provide an estimated CR curve for each rate parameter. The likelihood function is updated by writing the mean and variance as functions of drug concentration. We use the four-parameter logistic function for modeling the CR for each rate although BESTDR is flexible to any statistical model. For a rate parameter, θ, the four-parameter logistic function is defined by θ_0 (the rate at concentration 0), θ_{inf} (the rate as the concentration goes to infinity), θ_{50} (the log-concentration when the rate is at the midpoint of θ_0 and θ_{inf}), and θ_h (the Hill coefficient or slope at θ_{50}). We enforce that all rates be positive by defining $d\theta$ as the difference between $\min(\theta_0, \theta_{inf})$ and $\max(\theta_0, \theta_{inf})$; that is, if the function is decreasing, then we estimate θ_{inf} and $d\theta$ and define $\theta_0 \equiv \theta_{inf} + d\theta$. Priors are provided for each of the four parameters of the curve from a zero-truncated normal distribution for the θ_0/θ_{inf}, $d\theta$, and θh and a normal distribution for θ_{50}. BESTDR uses Hamiltonian Monte Carlo to estimate posterior distributions for each parameter of each CR function. More mathematical details are provided in the Supplementary Appendix.

Simulation of *in silico* experiments

Simulations were performed using the R package estipop v0.0.1 (https://github.com/Michorlab/estipop). For each of the simulations, we defined parameters representing the rates in single-dose studies or the parameters of the curve in CR studies. When modeling CR curves, we generated rates at each tested drug concentration and generated cell count trajectories according to the underlying mechanistic process to use as data for estimation. We include details for each of the simulations along with priors used in the Extended Methods in the Supplementary Appendix.

Estimation of rates

Inference was performed using Stan v2.34.1 (https://mc-stan.org/) in the R package cmdstanr v0.7.1 (https://mc-stan.org/cmdstanr/) within our software package (32). We processed all data such that each observation contains the cell count at the current time for each type, the cell count for each type at the previous time, and the difference in time. The results from our estimation are samples from a posterior distribution that are summarized using the mean, variance, and confidence intervals (CI). Details for how to use the software to estimate rates are provided in the vignettes in the Supplementary Appendix.

Data preprocessing and analysis

Data preprocessing was performed in R v4.3.2 (RRID: SCR_001905) using the tidyverse v2.0.0 (RRID: SCR_019186) package for data manipulation and plotting.

HCT116 p53-VKI cell data

Lineage tracing data were downloaded and converted from lineage tracing over each time point to cell counts (33). We truncated the first 20 hours after treatment to account for the time required for the drug to take effect. The single-dose model used our single-dose birth–death process code for inference whereas the dose–response model used our logistic dose–response birth–death process code (included in the package and described in the Supplementary Appendix).

Hierarchical model data

Cell count time-course data for the multi-cell line, multidrug experiments were downloaded from the original database for datasets labeled as HTS001 (https://doi.org/10.5281/zenodo.18292966) as well as the small cell lung cancer (SCLC) dataset HTS031 (https://doi.org/10.5281/zenodo.18292966) provided alongside Thunor (34). For each condition, two technical replicates were performed for each cell line, dose, and drug combination over the 120 hours of the experiment. We preprocessed each dataset such that each observation contained the drug, cell line, dose, current and previous cell count, and time interval.

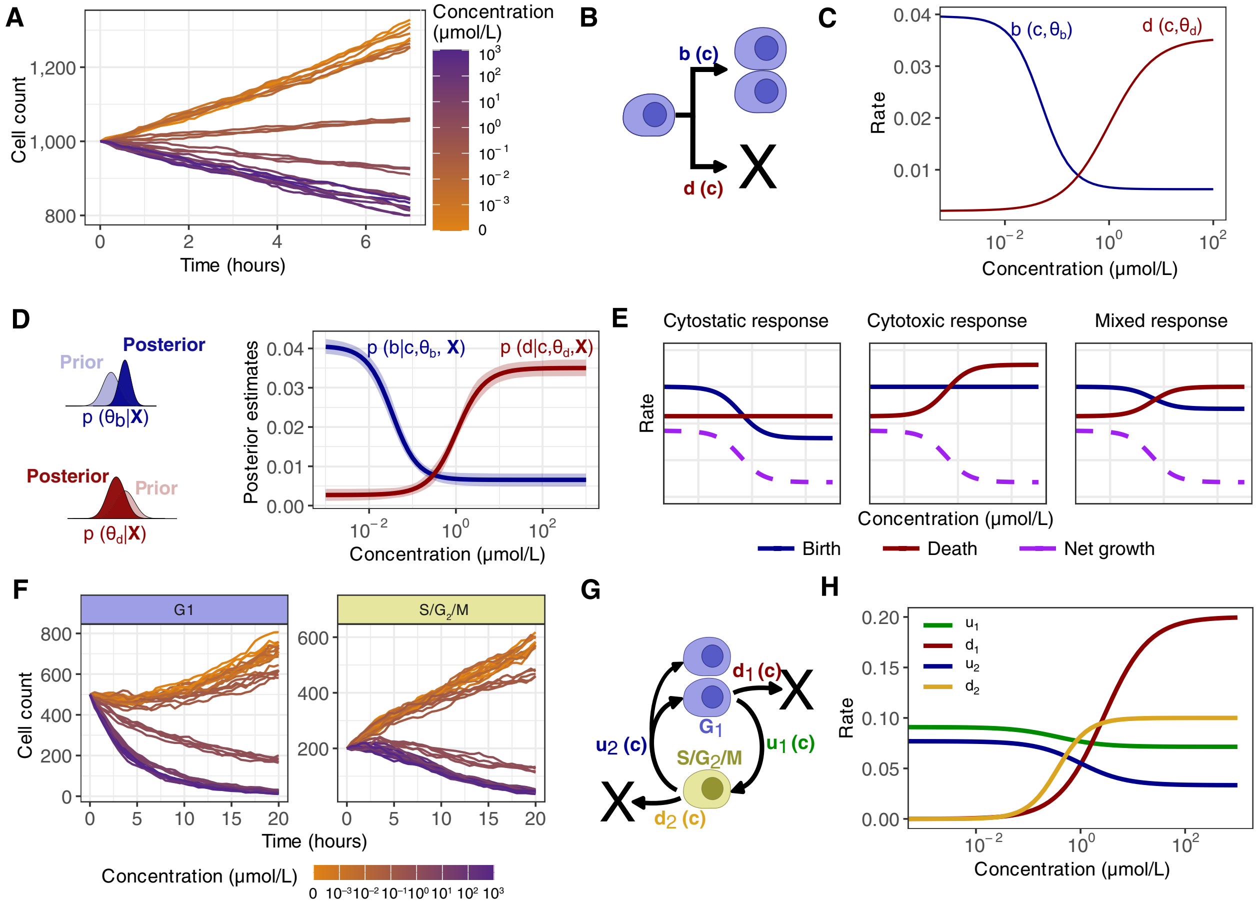

Figure 1.

BESTDR workflow uses viable cell counting data to inform a branching process model of cell growth in order to estimate CR parameters. **A,** Synthetic example of longitudinal cell counting data that are used to model the effects of drug concentration on cell growth in viable cells in which cell growth is observed in culture in the presence of varying drug concentrations. **B,** Branching process models are used to represent cell state transitions of individual cells fates for which each transition rate represents the rate of that event occurring in order to describe the population growth. A single type model describes cells that can undergo a cell division event at rate $b(c)$ or a death event at rate $d(c)$. **C,** Transition rates can be described by a CR function parameterized by unknown parameters that BESTDR attempts to estimate in order to estimate the function. **D,** BESTDR uses the model assumptions along with priors to update the normal likelihood model for cell counts, estimating each of the parameters of the CR curve. The resulting CR curve is a posterior distribution built on the posterior parameter estimates. **E,** Similar net growth curves (purple) can come from different birth and death rates that represent mechanisms of response to a drug. Cytostatic and cytotoxic responses are represented by changes in the birth and death rates, respectively, whereas a mixed response can also arise. BESTDR is able to distinguish these responses by estimating the separate curves. **F,** Cell state–specific phenotypes allow counting cells in individual states such as G_1 or $S/G_2/M$, which provides more dimensions of data to estimate specific drug effects. **G,** Multitype branching process models can define additional cell-specific events like cell phase transitions or phase-specific death. **H,** BESTDR includes multitype methods in the same framework to estimate state-specific transition rates and further understand how cell lines respond to drugs with respect to specific mechanisms.

Cell cycle dynamic model data

Cell count time-course data from *in vitro* experiments of cells treated with doxorubicin and gemcitabine at various concentrations were downloaded from the original database (26). For each condition, three technical replicates were performed, and cell counts were recorded every 30 minutes over 96 hours. We preprocessed each dataset such that each observation contained the drug, dose, current and previous cell count, and time interval.

Reprogramming dynamic model data

Cell count time-course data were obtained from *in vitro* reprogramming experiments comparing cells with and without the K36M mutation, which inhibits H3K36 methylation, significantly altering chromatin structure and transcriptional regulation. For each cell type, three independent biological experiments were conducted. Counts of Oct4-GFP+ (reprogrammed) cells and Oct4-GFP− (non-reprogrammed) cells were measured every 2 days between 0 and 4 days in culture . We preprocessed each dataset such that each observation contained the cell type, current and previous cell counts, and time interval.

Cell culture experiments

HCT116 p53-VKI cells (Lahav lab, Harvard Medical School) were seeded in 96-well plates and imaged using an Incucyte S3 imaging platform (RRID: SCR_023147). Cisplatin (CHEBI:27899) was added at increasing concentrations (maximum concentration of 25 μmol/L with a twofold increase for seven dose points: 0, 0.385 μmol/L, 0.770 μmol/L, 1.550 μmol/L, 3.125 μmol/L, 6.25 μmol/L, 12.50 μmol/L, and 25.0 μmol/L) 24 hours following cell seeding, and cells were grown under these conditions for 72 hours. Cells were not tested for *Mycoplasma* or authenticated before running experiments. Multiwell plates were imaged every 4 hours over the 72-hour period following addition of cisplatin. Dead cells were monitored using staining for ethidium bromide. Imaging was performed using a 10X objective to identify the total number of cells using the GFP channel (300 ms acquisition time) and dead cells using the red fluorescent protein channel (RFP; 400 ms acquisition time). The top-hat segmentation algorithm of the Incucyte S3 software platform was used to detect objects, including GFP+ (total cells) and GFP+ RFP+ (dead cells). We set the parameters for the GFP+ objects at a radius 30 μm and an intensity threshold of 0.1 and filtered for objects smaller than 100 μm^2, whereas the parameters for the RFP+ were set at a radius of 15 μm and an intensity threshold of 0.05 and filtered for objects smaller than 30 μm^2.

Results

BESTDR is a statistical framework for estimation of drug response

Standard viability assays (**Fig. 1A**) measure drug response by normalizing viable cell counts at each concentration and time point to control levels and then fitting a curve to estimate parameters like the IC_{50} (35, 36). However, these methods are sensitive to assay duration and experimental noise and offer limited mechanistic insights. To address these limitations, we developed BESTDR, a framework for estimating rate-based CR relationships from viability assay data. BESTDR models longitudinal cell counts across single or different states using a multitype CTMBP (**Fig. 1B**), in which each possible cell event (e.g., division, death, or state transition) occurs independently, with exponentially distributed waiting times (27). This framework captures the randomness of single-cell fate decisions while supporting tractable likelihood approximations.

Each event is governed by a rate function defined by a CR curve, parameterized by a set of variables, $\theta_x = (\theta_{x1}, \ldots, \theta_{xn})$ (**Fig. 1C**). Using observed cell counts, $\boldsymbol{X}(c, t)$, BESTDR estimates posterior distributions over these parameters, $p(\theta_x|c,\boldsymbol{X})$. In the single type setting, this refers to $p(b|c, \theta_b, \boldsymbol{X})$ and $p(d|c, \theta_d, \boldsymbol{X})$ (**Fig. 1D**). Parameter estimation is performed via Hamiltonian Monte Carlo (37, 38) using a multivariate normal likelihood function that only requires calculating the mean and variance (Materials and Methods; refs. 28, 31). Importantly, variance, typically treated as noise, captures underlying transition variability, enabling estimation of additional mechanistic parameters (**Fig. 1E**). Measurement error is modeled as an additive term in the variance (Materials and Methods; Supplementary Appendix). BESTDR provides a statistically rigorous and computationally efficient approach for estimating mechanistic drug response from standard viability assays.

Deconvolving cytostatic and cytotoxic drug responses *in silico*

To validate BESTDR, we conducted *in silico* simulations of cell growth and death under 12 drug concentrations. Each cell either divides into two daughters with rate $b(c)$ or dies with rate $d(c)$, in which c is the drug concentration. Changes in $b(c)$ or $d(c)$ reflect cytostatic and cytotoxic drug effects and can result in the same net growth curve when the division and death rates offset each other (**Fig. 1E**). BESTDR deconvolves the rate estimates separately using the viable cell count as input; the net growth rate is defined as the difference between birth and death rates. To account for technical variability, we introduced a 3% error to the observed cell counts, representing segmentation errors between observed and true cell counts that are similar to the accuracy of modern methods (39–41).

We simulated data by selecting parameters for the four-parameter logistic CR curves for the birth and death rates (Supplementary Table S1), which were used to calculate the birth and death rates at each concentration and simulate cell counts over time (**Fig. 2A**). Simulations were run for 72 hours with observations recorded every 4 hours to match standard experimental protocols. Using all time points, we estimated the birth and death rates at each concentration independently to assess whether BESTDR could accurately recapitulate cell growth dynamics from the data. At each concentration, the true birth and death rates fell within the 90% credible intervals (Supplementary Fig. S1A; Supplementary Table S2). We then used BESTDR to estimate the CR curves using all concentrations. All parameters of the CR curves fell within the 90% credible intervals of the posterior distributions (Supplementary Fig. S1B; Supplementary Table S1). The largest relative errors between the true values and the posterior means were observed for the b_{50} (the concentration at which the birth rate is halfway between both asymptotes) and the Hill coefficient for the birth rate, b_h, with relative errors of approximately 12.7% and 14%, respectively (Supplementary Fig. S1B; Supplementary Table S1). Importantly, the 90% credible bands for both the birth and death rates encompassed the true parameter values across all concentrations (**Fig. 2B**). This finding demonstrates that BESTDR can accurately estimate dynamic rates and provides mechanism-specific insights about cell division and death beyond net growth.

We calculated the net growth rate as the difference between the estimated birth and death rates and compared it with the GR curve (22) derived from the same data (**Fig. 2C**). The average concentration at which the posterior net growth rate is 0 (NG_0) is 0.251 μmol/L [90% CI, (0.226–0.275) μmol/L], similar to the GR_0 of 0.264 μmol/L as expected as the NG_0 and GR_0 measure the same theoretical value. Our findings indicate that BESTDR accurately recapitulates summary statistics from *in silico* experiments while offering estimates of cell growth and death rates and drug efficacy in the original units of measurement (hour^{-1}) as opposed to a relative response, which is unitless as in the GR.

We further constructed a scenario in which the CR may increase by including a hormetic effect (elevated growth at low dose) in the birth rate function, leading to an elevated growth rate at low concentrations (Supplementary Fig. S1C). We simulated cell growth data for a birth–death process at 14 concentrations along these curves for 72 hours, recording observations every 4 hours. Cell viability at 24, 48, and 72 hours shows hormesis, with normalized counts increasing up to 1.5× the control at low concentrations before declining (Supplementary Fig. S1D). The effect becomes more pronounced over time, highlighting that viability is not time-invariant and that amplified hormesis may reflect subtle shifts in underlying dynamics. We used BESTDR to estimate the birth and death rates under a four-parameter logistic function and a Gaussian process prior similar to bdChemo (25), cubic B-splines, and a three-layer fully connected neural network with two heads to approximate the CR curve (Supplementary Fig. S1E, details in Materials and Methods and Supplementary Appendix). The four-parameter logistic function fails to capture the birth rate's nonmonotonicity, but the other curves within the BESTDR framework, especially the neural network, closely approximate it. This finding demonstrates BESTDR's flexibility in modeling complex CR dynamics without

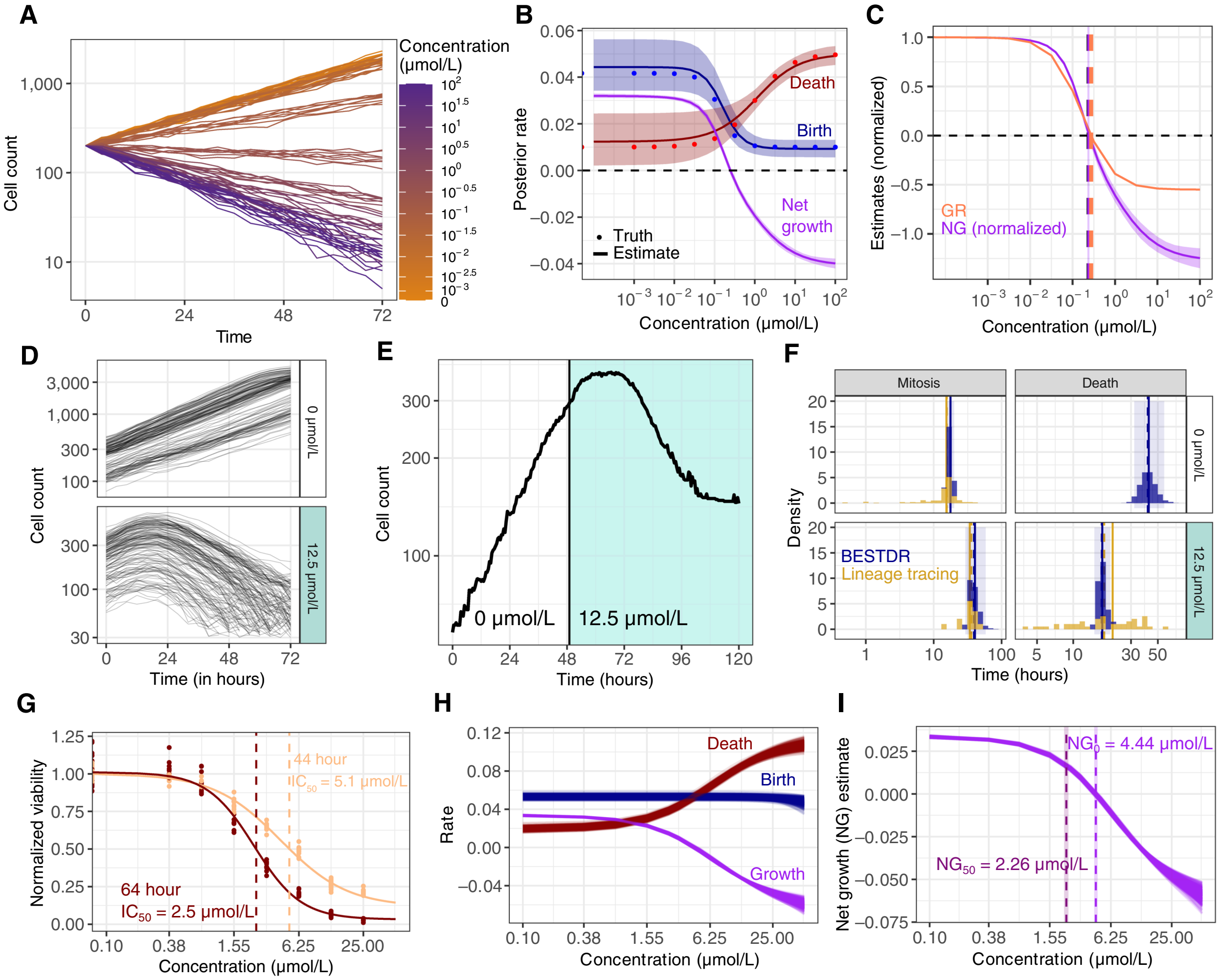

Figure 2.

BESTDR estimation can deconvolve birth and death rates in viable cell counting experiments. **A,** Simulation of longitudinal cell counts of cells undergoing division and death following a four-parameter CR curve at various concentrations. **B,** Posterior mean and 90% credible bands for the birth and death CR curves built from the posterior distributions for the parameters that accurately recapitulate the true concentration response as shown in **A**. **C,** Comparison between the net growth (NG; purple) and GR (orange) methods show similar predicted concentrations at which cell turnover is 0 based on the data in **A**. However, the total efficacy is different since net growth is in hour^{-1} units and provides a measure of the total change in cycling rate and growth rate is unitless as a measure of relative response. **D,** HCT116 p53-VKI cells were seeded and grown in cell culture for 72 hours in control (white) and 12.5 μmol/L cisplatin (turquoise) in 48 wells, recording viable cell count every 4 hours in three regions per well (dataset 1). **E,** Live-cell lineage-tracing experiments of HCT116 p53-VKI cells (dataset 2) recording that all cell fates have similar growth and response to cisplatin after treatment (turquoise), which is used to validate mitosis and death rates estimated from BESTDR. **F,** BESTDR estimates of the average time between mitosis and death events using only cell counts (blue) were compared to the distribution-realized mitosis and death times in the lineage-tracing data (gold), showing agreement in the distribution, with the medians (dashed lines) overlapping. **G,** Normalized viability estimates of a CR and the corresponding IC_{50} from HCT116 p53-VKI experiments at multiple concentrations. **H,** The birth (blue) and death (red) response curves show that cisplatin is primarily cytotoxic with little to no effect on cycling time. **I,** The net growth rate (purple) CR describes the change in cell turnover with increasing concentration. The NG_{50} is similar in value to the 72-hour IC_{50}, but the NG_0 is more informative as the concentration at which no net growth occurs.

relying on parametric or mechanistic assumptions. Further experiments show that BESTDR is able to distinguish between fully cytostatic, cytotoxic, or mixed responses (Supplementary Appendix Section 2).

BESTDR predicts *in vitro* cisplatin birth and death CR curves

To assess the performance of BESTDR with experimental data, we compared estimates obtained from two orthogonal experimental assays at different resolutions of data under control and treatment. First, we performed cell counting experiments over multiple replicates, recording only cell counts representing more typical HTS experiments for estimating drug response. Separately, we observed mitosis and death times in single-cell live-cell lineage-tracing experiments, which have higher resolution but lower throughput for a single replicate. To obtain the first dataset, HCT116 p53-VKI cells were treated with cisplatin and viable cell counts were recorded every 4 hours for 72 hours, without drug and with 12.5 μmol/L cisplatin, for multiple replicates (Materials and Methods). Cells grew exponentially in control and cisplatin but started undergoing apoptosis approximately 20 hours after treatment initiation (**Fig. 2D**). To obtain the second dataset (33, 42), HCT116 cells were cultured without cisplatin for 2 days, followed by cisplatin treatment at 12.5 μmol/L for 3 days; throughout the entire duration of the experiment, each cell's fate was tracked and recorded (Supplementary Fig. S1F). The two datasets are comparable in terms of the total number of viable cells at each time point, with the second dataset providing information on cell fates that are used to validate estimates obtained by BESTDR from the first dataset. We observed doubling times of 20.3 hours in dataset 1 versus 20 hours in dataset 2 in control conditions, and similar maximum cell counts at around 16 to 20 hours after treatment before the drug effect manifested in dataset 2, suggesting that the different methods of tracking cell growth yield comparable results (**Fig. 2D** and **E**).

Using BESTDR, we estimated the birth and death rates from the count data in dataset 1 and compared them with the time-to-mitosis and time-to-death distributions from dataset 2. The estimated mean time to mitosis was 17.6 hours (95% CI, 15.7–19.9) for control cells and 40.4 hours (95% CI, 29.2–58.0) for treated cells, which are similar to the lineage-tracing means of 15.4 and 34.0 hours, respectively (**Fig. 2F**). The estimated mean times to death under cisplatin were 42.0 hours (95% CI, 32.0–64.1) for control and 17.4 hours (95% CI, 15.0–21.4) for treated cells, compared with 21.2 hours observed in the lineage-tracing data. Although not all estimates fall exactly within the corresponding CIs, the differences are within the range expected given stochastic variation and differences in experimental design. In particular, lineage-tracing times are direct realizations from individual cells and thus may reflect higher biological and measurement noise than the model-based population-level estimates. Furthermore, the distribution of death times in the control condition could not be robustly estimated because of the low number of observed death events in that setting (**Fig. 2F**). Overall, these comparisons support the ability of BESTDR to recover key mechanistic features from bulk count data.

To investigate BESTDR's ability to estimate a CR curve, we treated HCT116 p53-VKI cells with eight concentrations of cisplatin and tracked viable counts for 72 hours, including the data from the previous experiment at 0 and 12 μmol/L (Supplementary Fig. S1G). Because of the 20-hour delay until manifestation of cisplatin's effect, we analyzed cell counts after 24 hours within higher concentrations to focus on the exponential growth phase, counting cells at 44 and 64 hours (20 and 40 hours after our initial time point). We chose a four-parameter logistic function to model the 20- and 40-hour viability curves, yielding an estimated IC_{50} of 5.1 and 2.5 μmol/L, respectively (**Fig. 2G**). The shift in IC_{50} underscores the limitations of normalized viability, which depends on the experimental stopping time and is not directly comparable with rate-based metrics. BESTDR revealed that the death rate increased with concentration over the range tested whereas the birth rate remained constant, changing by only about 0.001 hour^{-1} across the range. This observation suggests that cisplatin primarily induces apoptosis rather than inhibiting cell division, with a net difference in death rate of 0.080 hour^{-1} (**Fig. 2H**). This finding corroborates previous studies (43) and the lineage-tracing data, showing similar mitotic times but differing death rates between untreated and cisplatin-treated cells (Supplementary Fig. S1F).

We used BESTDR to estimate the concentration at which the net growth rate is half that of the control (NG_{50}) and 0 (NG_0), respectively. The NG_{50} was estimated as 2.26 μmol/L (90% CI, 2.16–2.37 μmol/L; **Fig. 2I**), which was comparable but lower than the IC_{50} of 2.5 μmol/L (**Fig. 2G**), whereas the NG_0 was estimated as 4.44 μmol/L (90% CI, 4.28–4.60 μmol/L; **Fig. 2I**). By revealing that cisplatin predominantly increases the death rate while keeping the cell birth rate largely unaffected, BESTDR offers valuable mechanistic insights into drug action.

Accounting for cell clearance in multitype models

We next investigated whether incorporating both viable and dead cell counts improves treatment response estimation compared with using viable counts alone. We analyzed *in silico* data obtained in a setting in which viable cells may divide or die with logistic CR functions, $b(c)$ and $d(c)$, and dead cells clear from the population at a constant rate, k (**Fig. 3A** and **B**). Clearance represents loss of adherence to the plate and disintegration of apoptotic cells; in those scenarios, cells are no longer counted and appear as a decrease in dead cell counts (44). We simulated cell growth during treatment at 10 different concentrations, tracking viable and dead cells with clearance set to zero (**Fig. 3C**) and 0.02 hour^{-1} (**Fig. 3D**) and added random noise (Supplementary Table S3). These data were used to estimate birth and death rates using (i) BESTDR applied to viable counts ("Live BESTDR"), (ii) BESTDR applied to viable and dead counts, accounting for dead cell clearance ("Live-dead BESTDR"), and (iii) the "Static/Toxic" GR ordinary differential equation (ODE) model (30), which estimates rates from viable and dead counts without clearance. When clearance was zero, all models closely fit the true birth and death rate curves. Live BESTDR also provided accurate estimates, with area between the curve (ABC) values of 0.023 (birth rate) and 0.029 (death rate) although with slightly wider credible intervals due to the use of only viable cell data (**Fig. 3E**; Supplementary Table S3). Live-dead BESTDR achieved similar fits, with ABC values of 0.005 (birth rate) and 0.001 (death rate) and 95% credible intervals encompassing the true curves (**Fig. 3F**). The Static/Toxic model had an ABC of 0.003 for the birth rate and 0.010 for the death rate, indicating high accuracy (**Fig. 3G**). These results suggest that live-cell counting alone is sufficient for estimating birth and death rates when there is no dead cell clearance.

When clearance was included, live BESTDR maintained similar levels of accuracy to the previous scenario, with ABC values of 0.025 (birth rate) and 0.028 (death rate, **Fig. 3H**). Live-dead BESTDR accurately recapitulated the original rates, with ABC values of 0.002 (birth rate) and 0.005 (death rate) and the true dose–response curves falling within the 95% credible intervals (**Fig. 3I**). In contrast, the ODE model's estimates deviated significantly from the true values at higher concentrations and even produced negative birth rates (**Fig. 3J**), with ABC values increasing to 0.126 (birth rate) and 0.128 (death rate). An ODE model that accounts for cell clearance is practically unidentifiable and produces noisy and potentially negative estimates for the rates.

Despite a slight increase in standard error of live-only BESTDR relative to live-dead BESTDR, all parameters in the BESTDR simulations fell within the 95% credible intervals (Supplementary Table S3). This finding illustrates that BESTDR models can effectively estimate birth and death rates even when dead cell clearance is unknown, outperforming ODE models that fail to account for clearance. These observations highlight BESTDR's robustness and practicality for analyzing cell growth data without the need for additional measurements of dead cells.

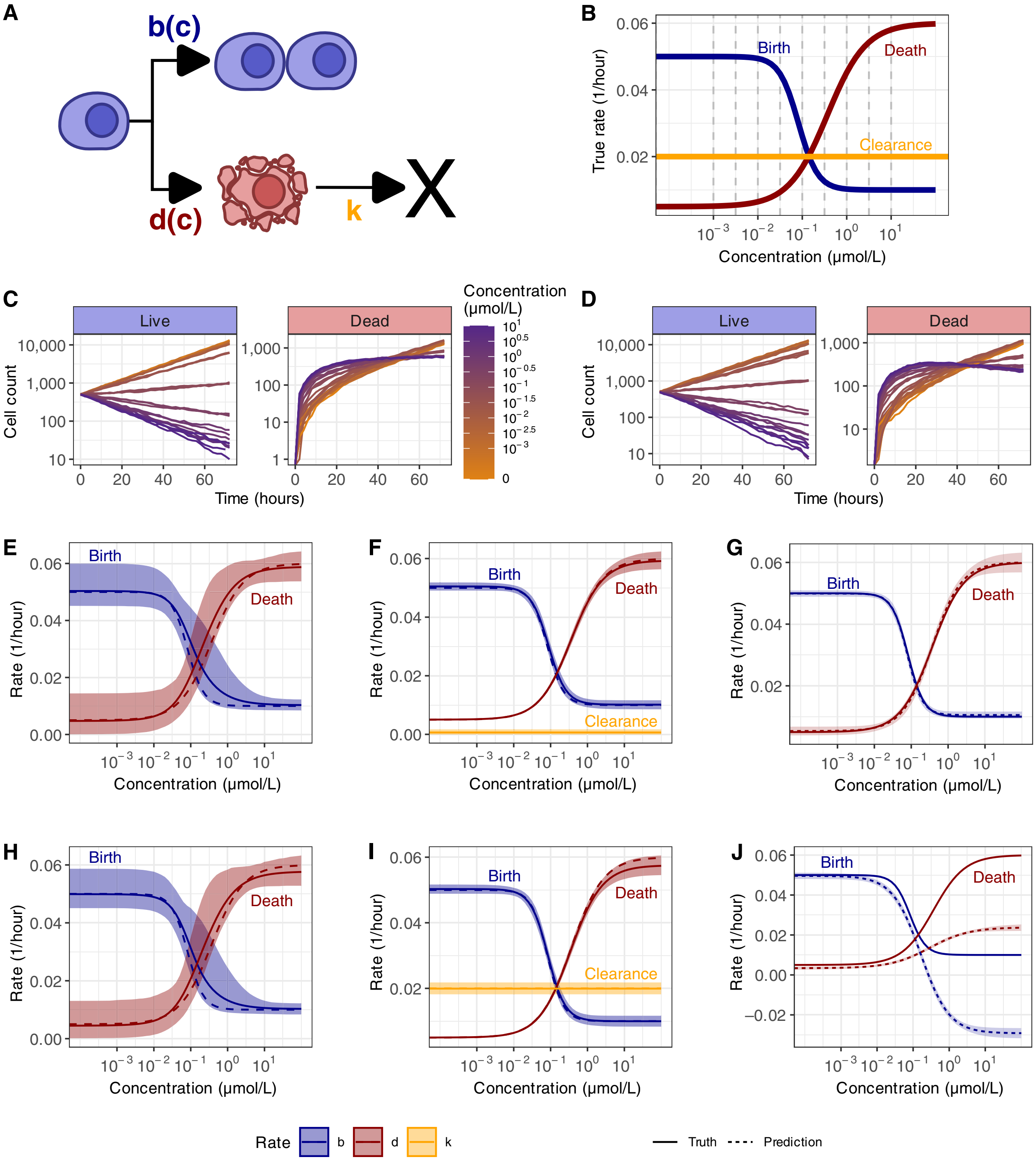

Figure 3.

Comparing estimation of birth and death rates using viable and dead cell counts based on simulated data. **A,** A model for cell growth and dead cell clearance. Viable cells can divide or die with concentration-dependent cell division and death rate functions $b(c)$ and $d(c)$, respectively, whereas dead cells clear with constant rate k independent of drug concentration. **B,** The CR for the birth and death rates are modeled as four-parameter logistic functions and constant clearance. **C,** Simulations of trajectories from a model with birth and death rates with no clearance ($k = 0$ hour^{-1}) and counting both viable and dead cells show a monotonically increasing dead cell count. **D,** A simulated scenario with clearance ($k = 0.02$ hour^{-1}) allows dead cell counts to decrease at higher concentrations when the number of viable cells also decreases. **E,** Live-only BESTDR estimates and 90% credible bands of the CR curves with data in which no clearance occurs. **F,** Live-dead BESTDR estimates and 90% credible bands of the CR curves with data in which no clearance occurs. **G,** Static-toxic GR estimates of the CR curves with data in which no clearance occurs. **H,** Live-only BESTDR estimates and 90% credible bands of the CR curves with data in which the true clearance rate is 0.02 hour^{-1}. **I,** Live-dead BESTDR estimates and 90% credible bands of the CR curves with data in which the true clearance rate is 0.02 hour^{-1}. **J,** Static-toxic GR estimates of the CR curves with data in which the true clearance rate is 0.02 hour^{-1}.

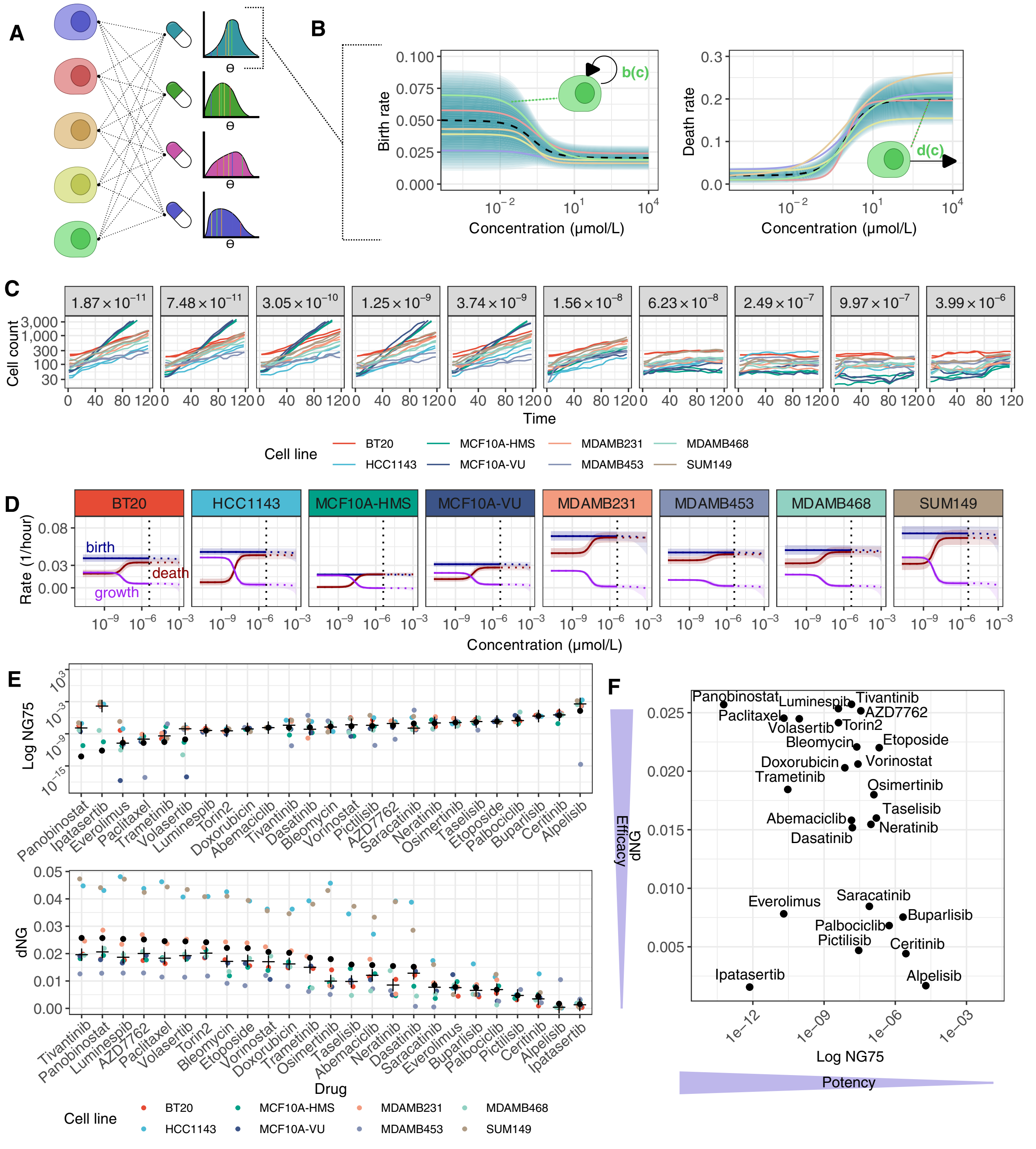

Figure 4.

Hierarchical mechanistic CR models use data from multiple cell lines for more robust estimates. **A,** High-throughput drug screens collect viability data across combinations of multiple cell lines for multiple drugs. The parameters for division and death, $b(c)$ and $d(c)$, respectively, that form the CR curve come from a distribution parameterized by hyperparameters, Θ. We model each cell line's birth and death rate parameters as realizations from distributions such that there is some similarity across cell lines of the same type. **B,** An individual cell line has birth and death CR curves that are realizations from a distribution of possible curves that is built from the hyperparameters for the parameters that describe each curve. **C,** Longitudinal cell counts over eight breast cancer cell lines show similar response to increasing concentration of doxorubicin, leading to similarity in overall dynamics. Each cell line is measured in two replicates at each drug over 120 hours. **D,** Cell line–specific estimates of the birth, death, and net growth CR curves that are estimated simultaneously in a hierarchical model, borrowing information across cell lines. **E,** Estimation of rate-specific parameters over all cell lines in each drug independently results in statistics for potency (NG_{75}) and efficacy (dNG) that can be used to compare drugs based on their response while accounting for the cell line–to-cell line

(*Continued on the following page.*)

Hierarchical modeling for high-throughput drug screens

We then extended the live-only BESTDR model to analyze high-throughput drug screens involving multiple cell lines. To account for cell line–specific diversity in drug responses, we modeled drug response of all cell lines in a hierarchical framework, which assumes that individual curves are related (4, 9, 17, 45). Cell growth follows a birth–death process (**Fig. 4A**), but the rate parameters are realized from shared probability distributions, reflecting common dynamics and drug responses across cell lines and resulting in cell line–specific curves for each rate (**Fig. 4B**). We applied this hierarchical model to response data from eight breast cancer cell lines treated with 25 drugs over concentrations ranging from 1.8×10^{-5} μmol/L to 3.9 μmol/L (34). Each drug was modeled with BESTDR independently, estimating cell line–specific parameters and hyperparameters specifying the shared distributions.

We set out to investigate cell response to doxorubicin over multiple cell lines with similar response using a hierarchical model (**Fig. 4C**). Previous studies and the Genomics of Drug Sensitivity in Cancer database reported a geometric mean IC_{50} of 0.336 μmol/L (range, 0.0098–19.6 μmol/L) for doxorubicin in breast cancer cell lines with a concentration range between 0.004 and 1.02 μmol/L (2), showing that large variability exists across cell lines in the same tissue type. In contrast, our dataset showed an average 96-hour IC_{50} of 0.018 μmol/L (range, 0.004–0.024 μmol/L) using traditional metrics. This discrepancy highlights inconsistencies when using IC_{50} values due to differences in experimental conditions like assay duration and reiterates the need for methods invariant to such variability. Additional sources for this discrepancy could be due to large cell line–to–cell line variability, which hierarchical models address.

As we observed continued cell growth even at the highest concentrations tested, we introduced two metrics to avoid extrapolation beyond the tested concentration range. First, we defined the NG_{75} as the concentration at which the growth rate is 75% of the control. Second, dNG is the net difference in growth rate between the control and the largest dose. We found that the average 96-hour IC_{25}, the concentration at which 25% growth inhibition is observed (equivalent to 75% of the control), had a mean of 9.4×10^{-3} μmol/L (range, (2.2×10^{-3}–7.1×10^{-2}). The BESTDR-determined average NG_{75} across cell lines was 7.5×10^{-3} μmol/L (range, (2.5×10^{-3}–1.5×10^{-2}) and the average dNG was 0.020 hour^{-1} (range, (0.008–0.036); **Fig. 4D**). These findings demonstrate that the potency values are similar to those from viability assays whereas efficacy is unaffected by experiment duration. The BESTDR-estimated curves (**Fig. 4D**) indicate that the primary response of breast cancer cell lines to doxorubicin over the concentration range tested is an increase in the death rate, whereas the birth rate remains nearly constant, suggesting that doxorubicin's mechanism of action is primarily cytotoxic (46).

To illustrate how BESTDR can be used to rank drugs for further investigation in high-throughput drug-screening experiments, we compared the potency and efficacy of 25 drugs across multiple cell lines. To account for cell line–specific effects, we used the NG_{75} and dNG statistics as determined by BESTDR (**Fig. 4E**). Drugs with lower NG_{75} values, such as panobinostat, reflect greater potency whereas drugs with higher dNG values reflect greater efficacy. The range of NG_{75} estimates for the grand mean across cell lines was 5.9×10^{-14} (panobinostat) to 1.9×10^{-5} (alpelisib). We then investigated the relationship between the two statistics, NG_{75} and dNG, for individual drugs across cell lines based on the mean of the hyperdistribution for each statistic, which is shared across all cell lines (**Fig. 4F**). The hierarchical model allows calculation of an average response across all cell lines by using the mean of the parameter distributions for each rate to construct CR curves (**Fig. 4F**). Additionally, we examined mechanism-specific responses across cell lines by defining the metrics B_{75} and dB for birth rates and D_{75} and dD for death rates, which refer to the concentration at which each rate is 75% of the control and the net difference between the control and largest dose, respectively (Supplementary Fig. S2A and S2B). For example, volasertib, a PLK1 inhibitor, which is known to lead to mitotic arrest, displayed a high dB and low B_{75}, indicating a primarily cytostatic effect by inhibiting cell division although it shows some cytotoxicity with a D_{75} of around 0.1 μmol/L, suggesting a mixed response as previously reported due to increased apoptotic activity (Supplementary Fig. S2A; refs. 47–49). In contrast, doxorubicin showed a high dD and low D_{75}, suggesting a predominantly cytotoxic response through increased cell death (Supplementary Fig. S2B).

To investigate the generalizability of BESTDR across HTS, we then analyzed data from two additional studies: one involving PC9-derived non–small cell lung cancer cell lines across 14 drugs (Supplementary Fig. S2C and S2D) and another with six SCLC cell lines across 138 agents (Supplementary Fig. S2E and S2F; refs. 34, 40, 50). In the PC9-derived cell line dataset, we observed minimal heterogeneity in drug response among cell lines, likely because they originated from the same parental cell line. The SCLC dataset exhibited greater heterogeneity, emphasizing the utility of using the mean response to account for variability across cell lines. Our analyses demonstrate that drug response data can be effectively summarized using scatterplots combining efficacy and potency metrics. For instance, in the PC9 study, paclitaxel emerged as the strongest drug when considering potency and efficacy equally, whereas seliciclib was the weakest (Supplementary Fig. S2D). In the SCLC dataset, most drugs clustered with low dNG and high NG_{75} values, indicating low efficacy and potency, but certain drugs, such as SCH-1473759, showed potential for further investigation based on its high potency and efficacy (Supplementary Fig. S2F).

These examples illustrate how hierarchical modeling with BESTDR can generate robust estimates by incorporating data from multiple experiments, even when conducted under different conditions. As the results are based on cell-intrinsic properties independent of experimental conditions, BESTDR provides consistent and reliable insights for drug ranking and selection in HTS.

Estimating transition rates between cell states across drugs

As many drugs target specific cell states or cycle phases, we next evaluated BESTDR's ability to estimate mechanism-specific drug responses in multistate systems. We used a simplified cell cycle model

(*Continued.*) variability. Drugs are ranked by the population mean across cell lines (black point) for that statistic and each cell line's statistic shows the between cell line variability in response, which will affect prediction of new cell line responses. Because of variability between cell lines, we include the median for each drug (+). **F,** Scatterplot of the average NG_{75} and dNG to show the drugs with the greatest response in the top left corner. Drugs previously discussed or having a high or low combination of potency and efficacy are labeled.

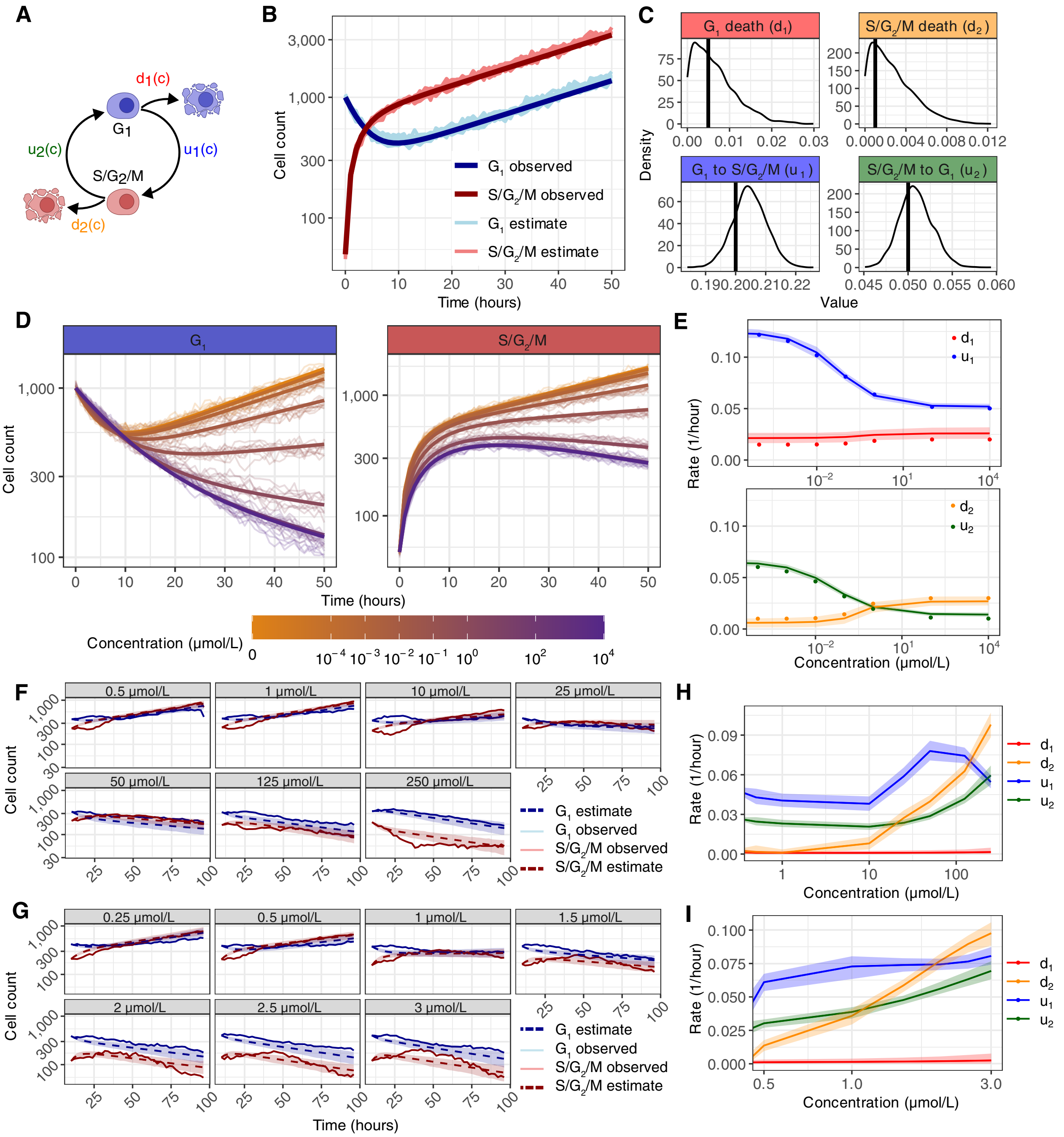

Figure 5.

Extending our framework to the cell cycle model allows us to capture the effects of different drugs on transition rates between cell cycle phases. **A,** Diagram of the cell cycle model. Here, we consider the G_1 phase (blue) and the combined S–G_2–M phase (red). With c representing drug concentration, we define the transition rates from G_1 to S/G_2/M and vice versa as $u_1(c)$ and $u_2(c)$, respectively, and the death rates for cells in the G_1 and S–G_2–M phases as $d_1(c)$ and $d_2(c)$, respectively. **B,** Synthetic data (light-colored lines) and deterministic estimates (dark-colored lines) obtained by simulating the cell cycle model under a single concentration, using as parameter values the mean of the estimated parameters. **C,** Posterior distributions of the estimated parameters. The black solid line indicates the parameter values used to generate the synthetic data. **D,** Synthetic data (light-colored lines) and deterministic trajectories (dark-colored lines) obtained by simulating the cell cycle model at multiple concentrations, using as parameter values the mean of the estimated parameters. **E,** Estimated parameters for the multiple-dose case using synthetic data using eight different concentration values. Parameter values

(*Continued on the following page.*)

distinguishing G_1 and S–G_2–M phases, based on a human DNA helicase B cell cycle reporter (26). We defined the G_1 to S–G_2–M transition rate as $u_1(c)$, the reverse as $u_2(c)$, and the death rates in G_1 and S/G_2/M as $d_1(c)$ and $d_2(c)$, respectively (**Fig. 5A**; Supplementary Appendix Section 1.5). To validate BESTDR, we simulated data for cell division and phase transitions under single- and multiple-dose scenarios to estimate the parameters (Supplementary Appendix, Section 1.5) and compared estimates to the ground truth. These analyses demonstrate that BESTDR accurately estimates death and transition rates between cell cycle phases (**Fig. 5B–E**). Posterior mean trajectories closely fit the simulated data, confirming BESTDR's predictive accuracy (**Fig. 5B**). In the single-dose setting, posterior peaks for each rate aligned with the true parameter values (**Fig. 5C**), and mean trajectories remained within the range of synthetic cell counts across concentrations (**Fig. 5D**). In multidose scenarios, BESTDR recovered the original logistic parameters, with true values falling within the 95% credible intervals (**Fig. 5E**; Supplementary Appendix, Section 1.4).

We then applied BESTDR, where each rate's CR function is modeled, with a Gaussian process prior to data from *in vitro* experiments of cells treated with doxorubicin or gemcitabine at various concentrations, counted every 30 minutes for 96 hours (26). Model-predicted trajectories of individual replicates were localized within prediction intervals (**Fig. 5F** and **G**), though deviations from the data occurred, likely because of effects of cell cycle synchronization early in the experiments. Prediction intervals for the other replicates showed similar effects (Supplementary Appendix Section 3). Posterior analysis revealed that both drugs increase the death rate of cells in S/G_2/M, with gemcitabine increasing the death rate more at lower concentrations (**Fig. 5H** and **I**). The slight increase in cycling rate occurs at higher concentrations but is slower than the death rate, leading to net decrease in count, suggesting possible hormesis-like effects, which could be tested with larger concentration ranges. The net rate effectively shows that gemcitabine strongly increases apoptosis during S-phase (**Fig. 5I**). Overall, these results support BESTDR's capacity to infer interpretable drug mechanisms from noisy, population-level data. Additional cell line and drug predictions are shown in the Supplementary Appendix (Section 3).

Quantifying reprogramming dynamics with BESTDR

Finally, we applied BESTDR to model induced cellular reprogramming, in which differentiated cells convert into induced pluripotent stem cells (iPSC) via constant overexpression of the transcription factors Oct4, Klf4, Sox2, and cMyc (OKSM; ref. 14). Differentiated cells (denoted as D) and iPSCs (denoted as SD) each have their own birth rates ($b_D(c)$ and $b_{SD}(c)$) and death rates ($d_D(c)$ and $d_{SD}(c)$), as well as an irreversible transition from D to SD cells at rate $r(c)$ (**Fig. 6A**; Supplementary Appendix Section 1.6; refs. 14, 51, 52).

To validate BESTDR in scenarios with reprogramming dynamics or irreversible transitions, we simulated single- and multiple-dose data with the transition/reprogramming rate increasing as the concentration increases, using a four-parameter logistic function for each rate (20 parameters; Supplementary Appendix Section 1.6). Unlike standard ODE models (Supplementary Appendix Equation 1.5) that only estimate net growth, BESTDR successfully recovered individual birth, death, and transition rates: the posterior means closely matched the input parameter values and fell within the 95% credible intervals for both single-dose (**Fig. 6B** and **C**) and multiple-dose scenarios (**Fig. 6D** and **E**).

We then applied BESTDR to experimental data of cells with and without the K36M mutation, which inhibits H3K36 methylation, significantly altering chromatin structure and transcriptional regulation and leading to faster reprogramming and a higher proportion of iPSCS relative to wild-type (WT) cells (14). Cell counts for nonreprogrammed (D) and reprogrammed (SD) cells were quantified via flow cytometry using an Oct4-GFP reporter (14). We used BESTDR to estimate the birth, death, and reprogramming rates of WT cells (**Fig. 6F**) and K36M-mutant cells (**Fig. 6G**). Although the predicted trajectories aligned with experimental trends, deviations were more pronounced in the K36M condition at intermediate time points, likely because of lower cell counts and increased stochastic variability, which can reduce the accuracy of population-level estimates in sparse datasets (**Fig. 6F** and **G**). However, later time points were similar to estimates, suggesting possible observation errors at the time points with low cell counts (**Fig. 6F** and **G**).

We found that birth and death rates were similar between WT and K36M-mutant cells, with the mutant-to-WT rate ratios ranging from 0.6 (95% CI, (0.43–0.79) to 1.33 (95% CI, (1.03–1.72); **Fig. 6H**). However, the K36M mutation increased the reprogramming rate 252-fold (95% CI, (8.36–1806.34); **Fig. 6H**). Trajectories generated from BESTDR estimates closely aligned with the experimental data (14), demonstrating that approximately 85% of K36M-mutant cells upregulated the pluripotent state reporter between days 4 and 8, compared with 5% of WT cells (**Fig. 6H**). BESTDR revealed that the K36M mutation primarily increases reprogramming rates with minimal impact on division or death. This finding demonstrates BESTDR's ability to quantify mutation-specific effects on reprogramming under OKSM overexpression.

Discussion

Measuring cellular drug response is essential in preclinical research to understand drug mechanisms. As technologies reveal ever-finer phenotypes, metrics beyond viability are needed to capture drug impacts on cell behavior. Here, we introduced BESTDR, a Bayesian framework that estimates concentration-response relationships from longitudinal cell count data in complex systems. It supports flexible model specification, mechanism-specific components, and hierarchical modeling for high-throughput screens. This design enables inference of dynamic processes such as cell cycling and state transitions, offering deeper insights than traditional approaches. Furthermore, as we computationally calculate the likelihood under the Central Limit Theorem, BESTDR is a more exact method for estimation than likelihood-free methods such as Approximate Bayesian Computation, which rely on simulation and selecting summary statistics to estimate parameters. BESTDR's outputs can also guide future experiments, including selection of drugs for combination therapy based on distinct mechanisms.

(*Continued.*) used to generate the synthetic data (dots) and estimated parameters, represented with their mean (solid line) and 95% credible interval (shade). **F,** Observed and estimated trajectories of cell cycle–specific counts under seven concentrations of doxorubicin. **G,** Observed and estimated trajectories of cell cycle–specific counts under seven concentrations of gemcitabine. **H,** Doxorubicin CR curves for each of the cell cycle rates estimated at each of the observed concentrations. **I,** Gemcitabine CR curves for each of the cell cycle rates estimated at each of the observed concentrations.

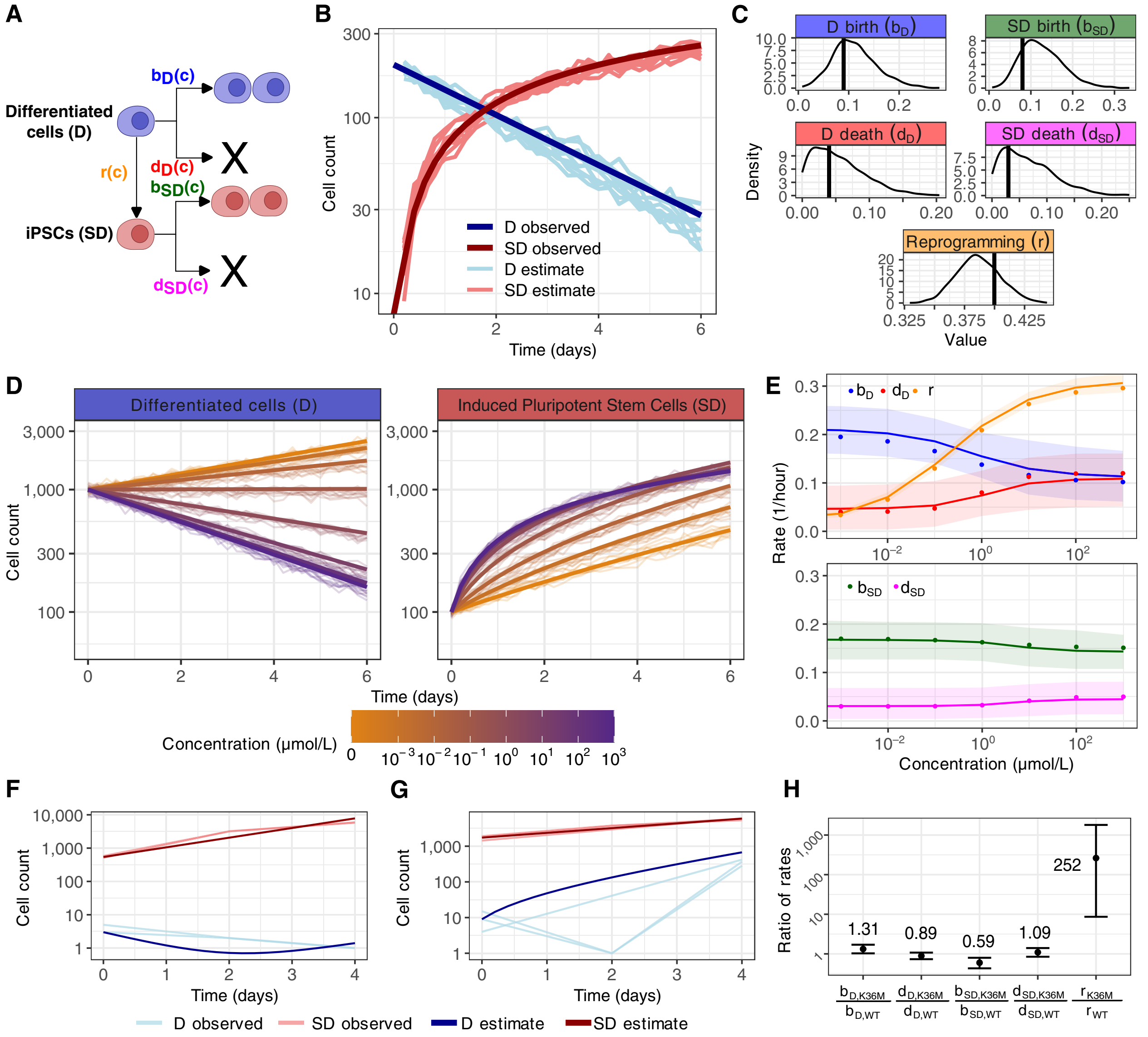

Figure 6.

Extending our framework to the reprogramming model allows us to compare the effectiveness of reprogramming approaches of different types of cells. **A,** Diagram of the reprogramming model with differentiated cells (D; blue) and iPSC cells (SD; red). With *c* representing drug concentration, we define birth rates as $b_1(c)$ and $b_2(c)$, death rates as $d_1(c)$ and $d_2(c)$, and the rate of the reprogramming process as $r(c)$. **B,** Synthetic data (dark) for estimation and deterministic trajectories (light) simulated from parameter estimates under the reprogramming model for a single cell type using BESTDR to estimate the specific rates at a single concentration. **C,** Posterior distributions of the estimated parameters. The black solid line indicates the parameter values used to generate the synthetic data. **D,** Synthetic data (dark) of a single cell type for estimation and deterministic trajectories (light) simulated from parameter estimates under the reprogramming model using BESTDR to estimate the specific rates under a CR curve for each of the five parameters for eight concentrations. **E,** True parameter values used to generate the synthetic data (dots) and estimated parameters, represented with their mean (solid line) and 95% credible interval (shade). **F,** Observed experimental data (light) and deterministic trajectories (dark) obtained from estimates in WT cells with OSKM over 4 hours. **G,** Observed experimental data (light) and deterministic trajectories (dark) obtained from estimates in K36M-mutant cells with OSKM over 4 hours. **H,** Estimates of the ratio between the value estimated for the cells with the K36M mutation and the value estimated for the WT cells.

Drug dose–response modeling is sensitive to data quality. Although BESTDR mitigates some errors of data generation through an added error term, high observation noise may inflate rate estimates as it cannot be fully disentangled from the intrinsic variability of the stochastic process. Advances in computational cell tracking could help reduce these errors (53–55). As a Bayesian framework, BESTDR is also influenced by prior choices and sample size, which affect accuracy and reliability (Supplementary Appendix). When modeling cell cycle dynamics, we observed that phase durations may deviate from an exponential distribution, with transient oscillations early in experiments before cells reach a stable phase distribution (26, 56). Methods exist to alleviate these exponential waiting time issues by employing the linear-chain trick, thereby allowing BESTDR to model nonexponential times, suggesting the need for testing a variety of possible models analogous to model selection in regression (54, 57–59). Finally, high-throughput drug screens may miss the concentration range in which drug response occurs, leading to flat CR curves and inaccurate metrics such as the NG_{50}. Different estimators such as NG_{75} are more reliable metrics without extrapolating. This limitation is common to all modeling and can be mitigated through dose-finding pilot experiments.

BESTDR offers a versatile and robust framework for dose–response modeling that leverages standard assays to uncover drug response mechanisms. Artificial intelligence (AI) and machine learning have transformed data analysis in pharmacology, complementing traditional modeling by enabling robust preprocessing and feature extraction, capabilities that enhance BESTDR's ability to model complex systems (60, 61). Algorithms that extract phenotypic features from live-cell imaging, such as morphology-based methods (54), can define cell states or types used as inputs for BESTDR to assess how drugs influence morphology. Importantly, BESTDR produces interpretable models, bridging the gap between AI-derived "black box" features and transparent mechanistic insights. We envision BESTDR as part of a hybrid pipeline combining AI-based morphologic or multiomics feature extraction with mechanistic modeling to yield deeper biological insights and more accurate predictions. By integrating AI and supporting rich cellular dynamics, BESTDR enables more informed experimental design and innovative drug development strategies. This holistic approach enhances our understanding of cellular responses and holds promise for accelerating therapeutic discovery.

Data Availability

All data analyzed in this study are publicly available or included in the article. Previously published datasets were used for analysis, and links to these data sources are provided in the text and Supplementary Appendix. High-throughput experimental data analyzed in this study are available from Zenodo at https://doi.org/10.5281/zenodo.18292967. The dataset generated from our cell line experiment has been included as Supplementary Data with this submission and is publicly available through figshare (doi:10.6084/m9.figshare.29610530). All software developed for this study is available on GitHub (https://github.com/olliemcdonald/bestdr).

Authors' Disclosures

T.O. McDonald reports grants from NIH/National Institute of General Medical Sciences R01GM144962 during the conduct of the study. F. Michor reports personal fees from Recursion Pharmaceuticals, Harbinger Health, and Zephyr AI outside the submitted work. No disclosures were reported by the other authors.

Authors' Contributions

T.O. McDonald: Conceptualization, data curation, software, formal analysis, funding acquisition, investigation, visualization, methodology, writing–original draft, writing–review and editing. **S. Bruno:** Software, formal analysis, validation, investigation, visualization, writing–original draft, writing–review and editing. **J.P. Roney:** Software, writing–review and editing. **I.K. Zervantonakis:** Data curation, investigation, writing–review and editing. **F. Michor:** Conceptualization, supervision, funding acquisition, writing–review and editing.

Acknowledgments

This research is supported by NIH/National Institute of General Medical Sciences grants R01GM144962 to T.O. McDonald and R35GM150815 to I.K. Zervantonakis. We gratefully acknowledge support of the Ludwig Center at Harvard and the Dana-Farber Cancer Institute's Center for Cancer Evolution. We also wish to thank Dr. Darren Tyson for his support and assistance with making the high-throughput screen experiments publicly available.

Note

Supplementary data for this article are available at Cancer Research Online (http://cancerres.aacrjournals.org/).

Received March 18, 2025; revised July 22, 2025; accepted November 13, 2025; posted first November 17, 2025.

References

1. McDermott U, Sharma SV, Settleman J. High-throughput lung cancer cell line screening for genotype-correlated sensitivity to an EGFR kinase inhibitor. Methods Enzymol 2008;438:331–41.
2. Yang W, Soares J, Greninger P, Edelman EJ, Lightfoot H, Forbes S, et al. Genomics of Drug Sensitivity in Cancer (GDSC): a resource for therapeutic biomarker discovery in cancer cells. Nucleic Acids Res 2013;41:D955–61.
3. Pushpakom S, Iorio F, Eyers PA, Escott KJ, Hopper S, Wells A, et al. Drug repurposing: progress, challenges and recommendations. Nat Rev Drug Discov 2019;18:41–58.
4. Corsello SM, Bittker JA, Liu Z, Gould J, McCarren P, Hirschman JE, et al. The Drug Repurposing Hub: a next-generation drug library and information resource. Nat Med 2017;23:405–8.
5. Wang R, Lin D-Y, Jiang Y. SCOPE: a normalization and copy-number estimation method for single-cell DNA sequencing. Cell Syst 2020;10:445–52.e6.
6. Attene-Ramos MS, Austin CP, Xia M. High throughput screening. In: Wexler P, editor. Encyclopedia of toxicology. Third ed. Oxford: Academic Press; 2014 [cited 2024 Dec 17]. p. 916–7. Available from: https://www.sciencedirect.com/science/article/pii/B9780123864543002098.
7. Mott BT, Eastman RT, Guha R, Sherlach KS, Siriwardana A, Shinn P, et al. High-throughput matrix screening identifies synergistic and antagonistic antimalarial drug combinations. Sci Rep 2015;5:13891.
8. Blay V, Tolani B, Ho SP, Arkin MR. High-throughput screening: today's biochemical and cell-based approaches. Drug Discov Today 2020;25:1807–21.
9. Nunes C, Anckaert J, De Vloed F, De Wyn J, Durinck K, Vandesompele J, et al. HTSplotter: an end-to-end data processing, analysis and visualisation tool for chemical and genetic in vitro perturbation screening. PLoS One 2024;19:e0296322.
10. Martinez-Serra J, Gutierrez A, Navarro-Palou M, Ros T, Amat JC, Marcus TF, et al. xCELLigence system for real-time label-free monitoring of growth and viability of cell lines from hematological malignancies. Onco Targets Ther 2014;7:985–94.
11. Single A, Beetham H, Telford BJ, Guilford P, Chen A. A comparison of real-time and endpoint cell viability assays for improved synthetic lethal drug validation. J Biomol Screen 2015;20:1286–93.
12. O'Clair L, Artymovich KA, Roddy M, Appledorn DM. Quantification of cytotoxicity using the IncuCyte ® cytotoxicity assay. Ann Arbor (MI): Essen Bioscience; 2014. p. 1–5. [Cited October 21, 2024.] Available from: https://api.semanticscholar.org/CorpusID:21740405.
13. Oki T, Mercier F, Kato H, Jung Y, McDonald TO, Spencer JA, et al. Imaging dynamic mTORC1 pathway activity in vivo reveals marked shifts that support time-specific inhibitor therapy in AML. Nat Commun 2021;12:245.
14. Hoetker MS, Yagi M, Di Stefano B, Langerman J, Cristea S, Wong LP, et al. H3K36 methylation maintains cell identity by regulating opposing lineage programmes. Nat Cell Biol 2023;25:1121–34.
15. Sakaue-Sawano A, Kurokawa H, Morimura T, Hanyu A, Hama H, Osawa H, et al. Visualizing spatiotemporal dynamics of multicellular cell-cycle progression. Cell 2008;132:487–98.
16. Meddings JB, Scott RB, Fick GH. Analysis and comparison of sigmoidal curves: application to dose-response data. Am J Physiol 1989;257:G982–9.
17. Fallahi-Sichani M, Honarnejad S, Heiser LM, Gray JW, Sorger PK. Metrics other than potency reveal systematic variation in responses to cancer drugs. Nat Chem Biol 2013;9:708–14.
18. Di Veroli GY, Fornari C, Goldlust I, Mills G, Koh SB, Bramhall JL, et al. An automated fitting procedure and software for dose-response curves with multiphasic features. Sci Rep 2015;5:14701.

19. Wang D, Hensman J, Kutkaite G, Toh TS, Galhoz A; GDSC Screening Team, et al. A statistical framework for assessing pharmacological responses and biomarkers using uncertainty estimates. Elife 2020;9:e60352.
20. Gutierrez J-JG, Lau E, Dharmapalan S, Parker M, Chen Y, Álvarez MA, et al. Multi-output prediction of dose–response curves enables drug repositioning and biomarker discovery. NPJ Precis Oncol 2024;8:209.
21. Chen Y, Zhang L. How much can deep learning improve prediction of the responses to drugs in cancer cell lines? Brief Bioinform 2022;23:bbab378.
22. Hafner M, Niepel M, Chung M, Sorger PK. Growth rate inhibition metrics correct for confounders in measuring sensitivity to cancer drugs. Nat Methods 2016;13:521–7.
23. Kummar S, Gutierrez M, Doroshow JH, Murgo AJ. Drug development in oncology: classical cytotoxics and molecularly targeted agents. Br J Clin Pharmacol 2006;62:15–26.
24. Harris LA, Frick PL, Garbett SP, Hardeman KN, Paudel BB, Lopez CF, et al. An unbiased metric of antiproliferative drug effect in vitro. Nat Methods 2016;13:497–500.
25. Liu Y, Crawford FW. Estimating dose-specific cell division and apoptosis rates from chemo-sensitivity experiments. Sci Rep 2018;8:2705.
26. Gross SM, Mohammadi F, Sanchez-Aguila C, Zhan PJ, Liby TA, Dane MA, et al. Analysis and modeling of cancer drug responses using cell cycle phase-specific rate effects. Nat Commun 2023;14:3450.
27. Kimmel M, Axelrod DE. Branching processes in biology [Internet]. New York (NY): Springer New York; 2015 [cited 2024 Oct 21]. Available from: https://link.springer.com/10.1007/978-1-4939-1559-0.
28. Roney JP, Ferlic J, Michor F, McDonald TO. ESTIpop: a computational tool to simulate and estimate parameters for continuous-time Markov branching processes. Bioinformatics 2020;36:4372–3.
29. McDonald TO, Cheng Y-C, Graser C, Nicol PB, Temko D, Michor F. Computational approaches to modelling and optimizing cancer treatment. Nat Rev Bioeng 2023;1:695–711.
30. Mills CE, Subramanian K, Hafner M, Niepel M, Gerosa L, Chung M, et al. Multiplexed and reproducible high content screening of live and fixed cells using dye drop. Nat Commun 2022;13:6918.
31. Yakovlev AY, Yanev NM. Relative frequencies in multitype branching processes. Ann Appl Probab 2009;19:1–14.
32. Carpenter B, Gelman A, Hoffman MD, Lee D, Goodrich B, Betancourt M, et al. Stan: a probabilistic programming language. J Stat Softw 2017;76:1.
33. Chakrabarti S, Paek AL, Reyes J, Lasick KA, Lahav G, Michor F. Hidden heterogeneity and circadian-controlled cell fate inferred from single cell lineages. Nat Commun 2018;9:5372.
34. Lubbock ALR, Harris LA, Quaranta V, Tyson DR, Lopez CF. Thunor: visualization and analysis of high-throughput dose–response datasets. Nucleic Acids Res 2021;49:W633–40.
35. Prinz H. Hill coefficients, dose–response curves and allosteric mechanisms. J Chem Biol 2010;3:37–44.
36. Kappenberg F, Brecklinghaus T, Albrecht W, Blum J, Van Der Wurp C, Leist M, et al. Handling deviating control values in concentration-response curves. Arch Toxicol 2020;94:3787–98.
37. Neal RM. MCMC using Hamiltonian dynamics. In: Handbook of Markov Chain Monte Carlo. Chapman and Hall/CRC; 2011. p. 113–62.
38. Betancourt M, Girolami M. Hamiltonian Monte Carlo for hierarchical models. In: Current trends in Bayesian methodology with applications. 1st ed. New York: Chapman and Hall/CRC; 2015. p. 79–101.
39. Edlund C, Jackson TR, Khalid N, Bevan N, Dale T, Dengel A, et al. LIVECell–a large-scale dataset for label-free live cell segmentation. Nat Methods 2021;18:1038–45.
40. Rundo L, Tangherloni A, Tyson DR, Betta R, Militello C, Spolaor S, et al. ACDC: automated cell detection and counting for time-lapse fluorescence microscopy. Appl Sci (Basel) 2020;10:6187.
41. Lin Y, Diao Y, Du Y, Zhang J, Li L, Liu P. Automatic cell counting for phase-contrast microscopic images based on a combination of Otsu and watershed segmentation method. Microsc Res Tech 2022;85:169–80.
42. Paek AL, Liu JC, Loewer A, Forrester WC, Lahav G. Cell-to-cell variation in p53 dynamics leads to fractional killing. Cell 2016;165:631–42.
43. Riddell IA. Cisplatin and oxaliplatin: our current understanding of their actions. Met Ions Life Sci 2018;18. doi:10.1515/9783110470734-007.
44. Costigan A, Hollville E, Martin SJ. Discriminating between apoptosis, necrosis, necroptosis, and ferroptosis by microscopy and flow cytometry. Curr Protoc 2023;3:e951.
45. Gelman A, Carlin JB, Stern HS, Rubin DB, editors. Bayesian data analysis. 2 ed. Boca Raton (FL): Chapman & Hall/CRC; 2004.
46. Nicoletto RE, Ofner CM. Cytotoxic mechanisms of doxorubicin at clinically relevant concentrations in breast cancer cells. Cancer Chemother Pharmacol 2022;89:285–311.
47. Nieto-Jiménez C, Alcaraz-Sanabria A, Pérez-Peña J, Corrales-Sánchez V, Serrano-Heras G, Galán-Moya EM, et al. Targeting basal-like breast tumors with bromodomain and extraterminal domain (BET) and polo-like kinase inhibitors. Oncotarget 2017;8:19478–90.
48. Vulin M, Jehanno C, Sethi A, Correia AL, Obradović MMS, Couto JP, et al. A high-throughput drug screen reveals means to differentiate triple-negative breast cancer. Oncogene 2022;41:4459–73.
49. Kats D, Ricker CA, Berlow NE, Noblet B, Nicolle D, Mevel K, et al. Volasertib preclinical activity in high-risk hepatoblastoma. Oncotarget 2019;10:6403–17.
50. Hayford CE, Tyson DR, Iii CJR, Frick PL, Quaranta V, Harris LA. An in vitro model of tumor heterogeneity resolves genetic, epigenetic, and stochastic sources of cell state variability. PLoS Biol 2021;19:e3000797.
51. Hanna J, Saha K, Pando B, Van Zon J, Lengner CJ, Creyghton MP, et al. Direct cell reprogramming is a stochastic process amenable to acceleration. Nature 2009;462:595–601.
52. Bruno S, Schlaeger TM, Del Vecchio D. Epigenetic OCT4 regulatory network: stochastic analysis of cellular reprogramming. NPJ Syst Biol Appl 2024;10:3.
53. Morelli R, Clissa L, Amici R, Cerri M, Hitrec T, Luppi M, et al. Automating cell counting in fluorescent microscopy through deep learning with c-ResUnet. Sci Rep 2021;11:22920.
54. Carpenter AE, Jones TR, Lamprecht MR, Clarke C, Kang IH, Friman O, et al. CellProfiler: image analysis software for identifying and quantifying cell phenotypes. Genome Biol 2006;7:R100.
55. Stringer C, Wang T, Michaelos M, Pachitariu M. Cellpose: a generalist algorithm for cellular segmentation. Nat Methods 2021;18:100–6.
56. Olofsson P, McDonald TO. A stochastic model of cell cycle desynchronization. Math Biosci 2010;223:97–104.
57. Bray M-A, Singh S, Han H, Davis CT, Borgeson B, Hartland C, et al. Cell painting, a high-content image-based assay for morphological profiling using multiplexed fluorescent dyes. Nat Protoc 2016;11:1757–74.
58. Marzec-Schmidt K, Ghosheh N, Stahlschmidt SR, Küppers-Munther B, Synnergren J, Ulfenborg B. Artificial intelligence supports automated characterization of differentiated human pluripotent stem cells. Stem Cells 2023;41:850–61.
59. Cimini BA, Chandrasekaran SN, Kost-Alimova M, Miller L, Goodale A, Fritchman B, et al. Optimizing the cell painting assay for image-based profiling. Nat Protoc 2023;18:1981–2013.
60. Zhang K, Yang X, Wang Y, Yu Y, Huang N, Li G, et al. Artificial intelligence in drug development. Nat Med 2025;31:45–59.
61. Li B, Tan K, Lao AR, Wang H, Zheng H, Zhang L. A comprehensive review of artificial intelligence for pharmacology research. Front. Genet. 2024;15:1450529. doi:10.3389/fgene.2024.1450529.